**Revision 1**

# Crocobelonite, $CaFe^{3+}_2(PO_4)_2O$, a new oxyphosphate mineral, the product of pyrolytic oxidation of natural phosphides

Sergey N. Britvin[1,2]*, Mikhail N. Murashko[1], Maria G. Krzhizhanovskaya[1], Natalia S. Vlasenko[3], Oleg S. Vereshchagin[1], Yevgeny Vapnik[4], and Vladimir N. Bocharov[3]

[1]Institute of Earth Sciences, Saint-Petersburg State University, Universitetskaya Nab. 7/9, St. Petersburg, 199034, Russia.

[2]Nanomaterials Research Center, Kola Science Center, Russian Academy of Sciences, Fersman Str. 14, Apatity, 184200, Russia.

[3]Geomodel Resource Center, Saint-Petersburg State University, Ulyanovskaya Str. 1, St. Petersburg, 198504, Russia.

[4]Department of Geological and Environmental Sciences, Ben-Gurion University of the Negev, POB 653, Beer-Sheva, 84105, Israel.

* Corresponding author. E-mail: sergei.britvin@spbu.ru

## Abstract

Crocobelonite, $CaFe_2^{3+}(PO_4)_2O$, is a new natural oxyphosphate discovered in the pyrometamorphic complexes of the Hatrurim Formation in Israel and Jordan. Crocobelonite-bearing assemblages contain a series of anhydrous Fe-Ni phosphates, hematite, diopside, anorthite, and phosphides – barringerite $Fe_2P$, transjordanite $Ni_2P$, murashkoite FeP, halamishite $Ni_5P_4$, and negevite $NiP_2$. Crocobelonite forms submillimeter-sized aggregates of prismatic to acicular crystals of saffron-red to pinkish-red colour. There are two polymorphic modifications of the mineral whose structures are interrelated by the unit-cell twinning. Crocobelonite-2*O* is orthorhombic, *Pnma*, *a* 14.2757(1), *b* 6.3832(1), *c* 7.3169(1) Å, *V* 666.76(1) Å$^3$, *Z* = 4. This polymorphic modification is isotypic with synthetic oxyphosphates $AV^{3+}_2(PO_4)_2O$ where *A* = Ca, Sr, Cd. The crystal structure has been refined to $R_B$ = 0.71% based on the powder XRD data, using the Rietveld method and the input structural model obtained from the single-crystal study. Chemical composition (electron microprobe, wt.%) is: CaO 16.03, MgO 0.56, $Fe_2O_3$ 43.37, $Al_2O_3$ 0.33, $SiO_2$ 0.32, $P_2O_5$ 39.45, Total 100.06. The empirical formula based on O = 9 *apfu* is $Ca_{1.02}(Fe^{3+}_{1.94}Mg_{0.05}Al_{0.02})_{2.01}(P_{1.98}Si_{0.02})_{2.00}O_{9.00}$ with $D_{calc.}$ = 3.555 g cm$^{-3}$. The strongest lines of powder XRD pattern [*d*(Å)(*I*)(*hkl*)] are: 6.54(16)(200), 5.12(26)(201), 3.549(100)(102), 3.200(50)(401), 2.912(19)(220), 2.869(40)(411), 2.662(21)(501). Crocobelonite-1*M* is monoclinic, $P2_1/m$, *a* 7.2447(2), *b* 6.3832(1), *c* 7.3993(2) Å, β 106.401(2)°, *V* 328.252(14) Å$^3$, *Z* = 2. This polymorphic modification does not have direct structural analogues. Its crystal structure has been solved and refined based on the single-crystal data to $R_1$ = 1.81%. Chemical composition is: CaO 15.56, MgO 0.16, NiO 0.78, $Fe_2O_3$ 41.28, $Al_2O_3$ 0.45, $V_2O_3$ 0.42, $Cr_2O_3$ 0.23, $TiO_2$ 0.79, $P_2O_5$ 39.94, Total 99.61, corresponding to the empirical formula (O = 9 *apfu*) $Ca_{0.99}(Fe^{3+}_{1.85}Ni_{0.04}Ti_{0.04}Al_{0.03}V^{3+}_{0.02}Cr_{0.01}Mg_{0.01})_{2.00}P_{2.01}O_{9.00}$ with $D_{calc.}$ = 3.604 g cm$^{-3}$. The strongest lines of powder XRD pattern [*d*(Å)(*I*)(*hkl*)] are: 6.98(17)(100), 4.40(22)(101), 3.547(100)(–201), 3.485(21)(200), 3.195(50)(020), 2.855(38)(102), 2.389(33)(–122). Crocobelonite

45 represents a specific novel type of phosphate mineralization formed by oxidation of phosphide
46 minerals at temperatures higher than 1000 °C and near-atmospheric pressure (pyrolytic oxidation).
47
48 **Keywords:** phosphate, oxyphosphate, oxophosphate, phosphide, pyrolytic oxidation, crystal
49 structure, new mineral, pyrometamorphism, Dead Sea, Middle East, Hatrurim Formation
50
51

This is the peer-reviewed, final accepted version for American Mineralogist, published by the Mineralogical Society of America.
The published version is subject to change. Cite as Authors (Year) Title. American Mineralogist, in press.
DOI: https://doi.org/10.2138/am-2022-8757. http://www.minsocam.org/

## Introduction

Since the discovery of combusted sedimentary beds in the Judean Desert (Picard 1931) and the recognition of similar rocks elsewhere in Israel, Palestinian Authority and Jordan (Bentor et al.1963; Gross 1977; Khoury and Nassir 1982a,b; Burg et al. 1992), pyrometamorphic complex known as the Hatrurim Formation or the Mottled Zone (Fig. 1) attracts substantial mineralogical interest. A combination of high-temperature combustion processes, intense hydrothermal activity and weathering in a desert climate have lead to the emergence of dozens of exotic mineral species (e.g., Sokol et al. 2014, 2019; Britvin et al. 2015, 2022a; Khoury 2020). As an example, the anomalous chromium mineralization is represented by a suite of $Cr^{3+}$ species, such as bentorite $Ca_6Cr_2(SO_4)_3(OH)_{12}\cdot 26H_2O$ (Gross 1980) and ellinaite $CaCr_2O_4$ (Sharygin et al. 2021; Galuskina et al. 2021a), along with chromates – chromatite $CaCrO_4$ (Eckhardt and Heimbach 1963), hashemite $BaCrO_4$ (Hauff et al. 1983), and siwaqaite, $Ca_6Al_2(CrO_4)_3(OH)_{12}\cdot 26H_2O$ (Juroszek et al. 2020). Selenium is being incorporated into selenides ($Se^{2-}$) (Sokol et al. 2014) and selenates ($SeO_4^{2-}$) (Juroszek et al. 2020). Calcium, the classic lithophile element, forms sulfides – oldhamite CaS and dzierżanowskite, $CaCu_2S_2$ (Galuskina et al. 2017). Other mineralogical highlights include oxides, such as grossite, $CaAl_4O_7$, discovered simultaneously in the Hatrurim Formation and within calcium-aluminium inclusions (CAI) of carbonaceous chondrites (Weber and Bischoff 1994); perovskite-supergroup minerals: vapnikite – the double perovskite $CaCaUO_6$ (Galuskin et al. 2014), shulamitite $Ca_3TiFe^{3+}AlO_8$ (Sharygin et al. 2013), cubic oxygen-deficient perovskite $Ca(Ti,Si,Cr)O_{3-\delta}$ (Britvin et al. 2022c), and aluminate garnet priscillagrewite-(Y), $(Ca_2Y)Zr_2(AlO_4)_3$ (Galuskina et al. 2021b).

Pyrometamorphic rocks of the Hatrurim Formation are enriched in phosphorus (e.g., Al-Ajarmeh and Khoury 2018), which can appear in the form of phosphides – rare minerals containing this element in a negative oxidation state (Britvin et al. 2015). To date, twelve phosphide minerals,

including nine new species, were recognized in Israel and Jordan. In the course of an ongoing research of phosphide assemblages, the authors of the present paper have discovered a suite of natural phosphates genetically related to phosphides (Britvin et al. 2021a). We herein introduce the reader with the most abundant representative of this mineralization – a new oxyphosphate $CaFe^{3+}_2(PO_4)_2O$. The mineral was named crocobelonite, from Greek κρόκος (saffron) and βελόνα (needle), for the orange-red colour and prismatic to acicular habit of its crystals. Both the mineral and the name have been approved by the Commission on New Minerals, Nomenclature and Classification (CNMNC) of the International Mineralogical Association (IMA 2020-005). Since the IMA approval of crocobelonite, it was found that the mineral could form two polymorphic modifications. The originally described polymorph (IMA 2020-005) crystallizes in the orthorhombic symmetry. The subsequently discovered monoclinic dimorph was proposed by the authors and submitted for voting to CNMNC as a distinct species (IMA 2021-038). However, based on the topological similarity of the crystal structures of both polymorphs (Nickel and Grice 1998), CNMNC has decided to leave the same root name (i.e., crocobelonite) for both polymorphic modifications. According to the CNMNC decision based on voting results, the orthorhombic dimorph (IMA 2021-038) was named crocobelonite-2*O*, whereas its monoclinic counterpart has got the name crocobelonite-1*M*. According to the Strunz classification (Strunz and Nickel 2001), crocobelonite belongs to the group 8.AC - anhydrous phosphates with additional anions, and with medium-sized and large cations. Within the Dana's system of mineralogy (Gaines et al. 1997), crocobelonite is related to the group 38.05 (anhydrous phosphates, etc with miscellaneous formulae). The holotype specimens of crocobelonite-2*O* (registration number 5559/1) and crocobelonite-1*M* (5683/1) are deposited in the collections of the Fersman Mineralogical Museum of the Russian Academy of Sciences, Moscow, Russia.

This is the peer-reviewed, final accepted version for American Mineralogist, published by the Mineralogical Society of America.
The published version is subject to change. Cite as Authors (Year) Title. American Mineralogist, in press.
DOI: https://doi.org/10.2138/am-2022-8757. http://www.minsocam.org/

## Geological setting and occurrence

The outcrops of pyrometamorphic rocks belonging to the Hatrurim Formation are sporadically exposed over the area of 150×200 km$^2$ surrounding the Dead Sea basin, and to the north, along the Jordan River valley to the Jordan-Syria-Israel border junction (Fig. 1). From a tectonic point of view, this area belongs to the Dead Sea Transform fault system (Garfunkel and Ben-Avraham 1996; Ben-Avraham et al. 2008). The reviews in geology and stratigraphy of this region can be found elsewhere (Burg et al. 1992; Fleurance et al. 2013; Abzalov et al. 2015). The sediments subjected to pyrometamorphic processes were represented by chalky-marly sequences of late Cretaceous to Eocene age. A brief stratigraphic overview and relationships between the sequences in Israel and Jordan can be found in Britvin et al. (2022b). The geological dating of combusted rocks gave controversial results, from 16 Ma to 250 Ka (Gur et al. 1995; Kolodny et al., 2014); the former value is approximately coincident with the onset of tectonic activity at the Dead Sea Transform Fault. The wide range of age dating may evidence for multiple pyrometamorphic events occurred in the region. The temperatures during combustion processes could attain 1450 °C (Sharygin et al. 2016), that lead to the calcination and even fusion of sedimentary beds, with formation of varicoloured marbles, hornfels and the so-called paralava – fused counterparts of igneous rocks (Vapnik et al. 2007). There is an overall consensus that pyrometamorphic processes were driven by the combustion of organic matter, but the definition and the origin of this organic substance remains obscure, varying from bitumen (e.g., Kolodny and Gross 1974) to oil gas (methane) (Novikov et al. 2013). The possible initial event that could trigger combustion processes over such a vast area is also obscure (Britvin et al. 2021b, 2022c).

The known enrichment of pyrometamorphic rocks of the Mottled Zone in phosphorus can be relied upon the entrapment of underlying phosphorite beds, which are widespread in this area (Nathan et al. 1979; Abzalov et al. 2015; Khoury 2019). Phosphorite xenoliths of black colour,

124 partially assimilated by varicoloured hornfels, can be found in phosphorite and stone quarries, which
125 tip the hills belonging to the Hatrurim Formation in the Daba-Siwaqa complex, West Jordan (Fig.
126 2ab). A deeper metamorphic transformation of entrapped phosphorites resulted in the emergence of
127 fine-grained fluorapatite (e.g., Al-Ajarmeh and Khoury 2018). The latter has an intense blue-green
128 to emerald-green colour due to the trace amounts of $Cr^{3+}$ in its composition (Fig 2c). Fluorapatite is
129 considered a likely source of phosphorus, which was required for phosphides formation (Britvin et
130 al. 2015, 2021a).

131 The type locality for crocobelonite-2*O* is a small abandoned quarry formerly operated for
132 phosphorites, located at the Daba-Siwaqa complex in the Jizah District, Amman Governorate,
133 Jordan (31° 21' 52" N, 36° 10' 55" E) (Fig. 1 and 2a). In this quarry, phosphide-phosphate
134 assemblages containing crocobelonite are comprised by diopside paralava and appear as nests and
135 schlieren up to 30 cm in size situated in brown to red-colored hornfels (Fig. 2a). Macroscopically,
136 the paralava nests have pale-brown colour, whereas the areas enriched in phosphates are colored in
137 greenish-brown hues (Fig. 3a). The paralava consists of random to radial aggregates of colorless
138 long-prismatic diopside crystals up to 0.2×3 mm in size, cemented by late hydrothermal calcite and
139 hydrous calcium silicates (Fig. 3b,c). Diopside composition is close to pure $CaMgSi_2O_6$, with Fe and
140 Al impurities of less than 0.1 wt.%. Phosphates, including crocobelonite, form bubble-like
141 segregations of brown color up to 1 cm size, disseminated in paralava. In thin sections, these
142 bubbles exhibit very inhomogeneous interior (Fig 3d). They are filled with aggregates of round
143 grains 0.05-0.5 mm in size, whose internal texture (Fig. 3e) resembles that of radial and
144 cryptocrystalline chondrules of chondritic meteorites (e.g., Kurat 1969; Grossman et al. 2000). The
145 droplets are composed of calcium silico-phosphate glass and unidentified anhydrous calcium silico-
146 phosphates; the mesostasis between the droplets has the similar composition. The peripheral rims of
147 centimeter-sized bubbles are composed of microcrystalline hematite, phosphides – murashkoite FeP

(Britvin et al. 2019b), zuktamrurite $FeP_2$ (Britvin et al. 2019a), barringerite $Fe_2P$ and transjordanite $Ni_2P$ (Britvin et al. 2020a), halamishite $Ni_5P_4$, negevite $NiP_2$ (Britvin et al. 2020b,c) and a variety of anhydrous phosphates (Fig. 3f), of which crocobelonite is the most abundant.

Crocobelonite-1*M* was primarily recognized in phosphide-phosphate assemblages encountered in detrital blocks of diopside paralava collected at the Halamish wadi, the Hatrurim Basin, Negev desert, Israel. The detailed description of this locality was recently reported by Britvin et al. (2022b). The specimens from the Hatrurim Basin do not contain bubble-like phosphate-phosphide aggregates, but in other terms are very similar to the samples from the Jordan locality. Subsequent investigations have revealed that both polymorphic modifications of crocobelonite occur together in the samples collected in Jordan and Israel.

## Analytical Methods

***Electron microprobe analysis (EMPA) and electron backscatter diffraction (EBSD)***

Determinations of the chemical composition were carried out on polished and carbon-coated sections using a Hitachi S-3400N scanning electron microscope equipped with an INCA WAVE 500 WDX spectrometer (20 kV, 10 nA), using the following standards (*K*α series lines): diopside (Ca, Si), rutile (Ti), chromite (Cr), V metal (V), hematite (Fe), trevorite (Ni), gehlenite (Al), and chlorapatite (P). EBSD phase determination and mapping was performed on the same polished sections, after reactive ion etching (RIE) with $Ar^+$ by means of an Oxford Instruments IonFab-300 instrument (500 V, 2.4 mA $cm^{-2}$ flow current). EBSD patterns were obtained using an Oxford Instruments Nordlys-HKL EBSD detector (20 kV, 1.5 nA, focused beam mode, 70° tilted stage) attached to a Hitachi S-3400N scanning electron microscope. Phase identification was carried out using the atomic coordinates obtained from X-ray structural refinements.

This is the peer-reviewed, final accepted version for American Mineralogist, published by the Mineralogical Society of America.
The published version is subject to change. Cite as Authors (Year) Title. American Mineralogist, in press.
DOI: https://doi.org/10.2138/am-2022-8757. http://www.minsocam.org/

172 ***Powder X-ray diffraction (PXRD) and Rietveld refinement***

173 PXRD patterns were obtained by means of a Rigaku RAXIS Rapid II diffractometer. The instrument
174 was equipped with a rotating anode (Co*K*α, 40 kV, 15 mA), microfocus mirror monochromator and
175 semi-cylindrical imaging plate detector ($r$ = 127.4 mm). The images were acquired in a Debye-
176 Scherrer geometry. A plate-to-profile data conversion was carried out using osc2xrd software
177 (Britvin et al. 2017). The unit-cell parameters refinement and calculation of theoretical patterns was
178 performed with Stoe WinXPOW software (Stoe and Cie GmbH). Rietveld refinement of PXRD
179 profile of crocobelonite-2*O* was carried out with Bruker TOPAS v.5.0 software (Bruker AXS).

180 ***Single-crystal X-ray diffraction (SCXRD) and crystal structures***

181 SCXRD studies were carried out for both crocobelonite polymorphs. Data collection for
182 crocobelonite-2*O* was performed using a Bruker Kappa APEX DUO CCD diffractometer
183 (microfocus tube, Mo*K*α radiation). Data collection for crocobelonite-1*M* was carried out with a
184 Rigaku Oxford Diffraction XtaLAB Synergy-S diffractometer equipped with a microfocus X-ray
185 tube (Mo*K*α) and HyPix-6000 hybrid photon counting detector. Data processing and integration
186 routines were completed using Rigaku Oxford Diffraction CrysAlisPro program suite (Rigaku
187 Oxford Diffraction 2018). The crystal structures were solved and refined with the *SHELX*-2018
188 package (Sheldrick 2015) via Olex2 graphical user interface (Dolomanov et al. 2009). The details of
189 data collection and structure refinement for both crocobelonite polymorphs can be retrieved from
190 crystallographic information files (CIF) in Supplementary Data. The SCXRD CIF file consists of
191 two datablocks. The first block contains the best SCXRD refinement results obtained for
192 crocobelonite-2*O*; these data were used as an input model for the Rietveld refinement of
193 crocobelonite-2*O*. The third datablock contains SCXRD refinement results for crocobelonite-1*M*.
194 Rietveld refinement results for crocobelonite-2*O* are given in the separate CIF file.
195

This is the peer-reviewed, final accepted version for American Mineralogist, published by the Mineralogical Society of America.
The published version is subject to change. Cite as Authors (Year) Title. American Mineralogist, in press.
DOI: https://doi.org/10.2138/am-2022-8757. http://www.minsocam.org/

196 ***Raman spectroscopy***

197 Raman spectra for both polymorphic modifications of crocobelonite were obtained from the X-ray
198 checked crystals, using a Horiba Jobin-Yvon LabRam HR800 spectrometer equipped with an Ar-ion
199 laser (5 mW, $\lambda = 514$ nm) and an Olympus BX41 microscope, using a 50× confocal objective.
200

201 **Appearance and physical properties**

202 Crocobelonite occurs as irregular dense segregations up to 0.5 mm, intergrown with diopside,
203 anorthite, hematite, phosphate-silicate glass and other phosphate minerals (Fig. 3f). Phosphides, in
204 general murashkoite FeP, zuktamrurite $FeP_2$, and the minerals belonging to the join barringerite
205 $Fe_2P$ - transjordanite $Ni_2P$, occur in the same areas. In the rarely found microcavities, crocobelonite
206 forms prismatic to acicular crystals reaching 30×150 μm in size (Fig. 4). The mineral has a saffron-
207 red (crocoite-like) colour in dense aggregates, whereas single crystals exhibit distinct dichroism
208 from pink-red to deep-red. Crocobelonite gives an orange strike and has a vitreous to greasy colour.
209 It is brittle and shows a perfect cleavage in two directions (crocobelonite-2*O*) and in one direction
210 (crocobelonite-1*M*), parallel to crystals elongation. Mohs hardness 4. The density, calculated based
211 on the empirical formula and unit-cell parameters, is 3.555 g $cm^{-3}$ (2*O* polymorph) and 3.604 g $cm^{-3}$
212 (1*M* polymorph). Crocobelonite-2*O* and crocobelonite-1*M* are visually indistinguishable from each
213 other, neither in macrosamples nor in thin sections. Moreover, they may occur in the same μm-sized
214 assemblages and even to form mutual intergrowths (Fig. 5). The most reliable method to distinguish
215 the polymorphs is the X-ray study. In polished thin sections, the 2*O* and 1*M* modifications can be
216 distinguished using electron backscatter diffraction (EBSD) (Fig. 5). Optical properties of
217 crocobelonite, measured in $AsBr_3$-S immersion liquids, are provided in Table 1.
218
219

This is the peer-reviewed, final accepted version for American Mineralogist, published by the Mineralogical Society of America.
The published version is subject to change. Cite as Authors (Year) Title. American Mineralogist, in press.
DOI: https://doi.org/10.2138/am-2022-8757. http://www.minsocam.org/

## Chemical composition

Crocobelonite shows rather uniform composition; chemical zoning has never been observed. EMPA data for holotype material of both polymorphic modifications are summarized in Table 2. Iron is calculated as $Fe^{3+}$ according to charge balance, taking into account the absence of water (Raman spectroscopy results) and crystal structure determinations which require the presence of 9 oxygen atoms per formula unit. The empirical formula of holotype crocobelonite-2*O* from Jordan (calculated on the basis of 9 O *apfu*) is $Ca_{1.02}(Fe^{3+}_{1.94}Mg_{0.05}Al_{0.02})_{2.01}(P_{1.98}Si_{0.02})_{2.00}O_{9.00}$; holotype crocobelonite-1*M* from Israel has the empirical formula $Ca_{0.99}(Fe^{3+}_{1.85}Ni_{0.04}Ti_{0.04}Al_{0.03}V^{3+}_{0.02}Cr_{0.01}Mg_{0.01})_{2.00}P_{2.01}O_{9.00}$. The ideal formula of crocobelonite is $CaFe^{3+}_2(PO_4)_2O$. The comparison of compositions reveals slightly elevated contents of transition metal impurities (Ni, V, Cr, Ti) in crocobelonite-1*M* from Israel. However, the presence of these impurities can not be considered as a factor which determines stabilization of monoclinic polymorph of crocobelonite. EMPA data obtained on the intergrowths of 2*O* and 1*M* polytypes show that they are indistinguishable by the chemical composition.

## Crystal structure and powder diffraction

X-ray single-crystal study of crocobelonite-2*O* showed that this polymorphic modification is isotypic with synthetic oxyphosphates of trivalent vanadium $AV_2O(PO_4)_2$, where $A$ = Cd, Ca, Sr (Boudin et al. 1994, 1995, 1996) (Table 3). However, the attempts of obtaining high quality SCXRD data for this polymorph were unsuccessful, due to the crystal splitting manifested by the appearance of electron density phantoms ($\geq 3$ *e* $Å^{-3}$) on the difference Fourier maps. In order to inspect the validity of SCXRD model, we have performed Rietveld refinement of powder diffraction profile of crocobelonite-2*O* (Fig. 6 and CIF file in Supplementary Information). The refinement has confirmed that this is a $Fe^{3+}$ analogue of synthetic compound $CaV^{3+}_2O(PO_4)_2$ (Boudin et al. 1994). Contrary to

the orthorhombic polymorph, crocobelonite-1*M* forms perfect crystals, which allowed conducting single-crystal structure solution and refinement. This polymorphic modification has no direct structural analogues, among neither natural nor synthetic phosphates. The crystal structures of both polymorphs show almost the same topology, with the same coordination of cation sites (Fig. 7, Table 4). Similar to synthetic phosphates $AV_2O(PO_4)_2$ (Boudin et al. 1996), crystal structures of crocobelonite-2*O* and -1*M* can be described as tridimensional frameworks $[Fe_2P_2O_9]^{\infty}$ composed of two kinds of structural subunits. The infinite chains (rods) of edge-sharing $Fe(1)O_6$ octahedra, propagating along the *b*-axis in both polymorphs (Fig. 7), have the same topology as $[TiO_6]$ rods in the rutile structure and hence are known as "rutile-like chains" (e.g., Baur 2007). The second type of subunit is comprised by the infinite chains $[Fe(2)PO_8]$, also running along the *b*-axis and composed of corner-sharing $Fe(2)O_6$ octahedra and $PO_4$ tetrahedra. Calcium atoms occupy the *b*-axis channels in the $[Fe_2P_2O_9]$ framework. The $P(1)O_4$ tetrahedron shares common edge with $Fe(1)O_6$ octahedron and common corners with $Fe(2)O_6$ octahedron. The $P(2)O_4$ tetrahedron is corner-sharing with two $Fe(1)O_6$ octahedra, $Fe(2)O_6$ octahedron and Ca-polyhedron (Fig. 8). The structural relationship between the polymorphs can be considered a type of "unit-cell twinning", well known in some silicate systems (e.g., Ito 1950; Yau and Peacor 1986). The differences between the unit-cell stacking in crocobelonite-2*O* and crocobelonite-1*M* are illustrated in Fig. 9. X-ray powder diffraction data for crocobelonite polymorphs are presented in Tables 5 and 6. The low- to mid-range regions of powder XRD profiles (Fig. 10) can be used to distinguish crocobelonite-2*O* from crocobelonite-1*M*.

## Raman spectroscopy

The Raman spectra of crocobelonite are shown in Fig. 11. The fingerprint regions (Fig. 11a) contain the groups of bands characteristic of inorganic orthophosphates (Table 7) (Nakamoto 2008, 2009).

The absence of bands in the O–H stretching region (3800–3000 $cm^{-1}$) and bending modes of molecular $H_2O$ (1630–1670 $cm^{-1}$) (Fig. 11b) evidences for the absence of water in the mineral composition, in accordance with the chemical, structural and optical data.

## Implications: crocobelonite and the new type of phosphate mineralization

Crocobelonite, $CaFe^{3+}_2(PO_4)_2O$, is an example of natural oxyphosphate (oxophosphate) – the mineral whose chemical formula contains the so-called "additional" oxygen atom(s) (e.g., Krivovichev 2008). Of more than 600 mineral species belonging to the phosphate class (Krivovichev 2021), oxyphosphates without other anions were, up to date, represented by three minerals: staněkite $(Fe^{3+},Mn^{2+},Fe^{2+},Mg)_2(PO_4)O$ (Keller et al. 1997), grattarolaite $Fe^{3+}_3(PO_4)O_3$ (Cipriani et al. 1997), and joosteite $Mn^{2+}(Mn^{3+},Fe^{3+})(PO_4)O$ (Keller et al. 2007). In contrast, the number of their nearest analogues – oxyarsenates (oxoarsenates) – approaches 20 minerals (Davis et al. 1965; Moore and Araki 1978; Vergasova et al. 2000; Roberts et al. 2001; Mills et al. 2010; Pekov et al. 2018, 2019a,b, 2021a,b; Shablinskii et al. 2018). The family of oxyarsenate minerals owes its diversity to a specific type of mineralization connected to arsenic-rich volcanic fumaroles, whose environment favours the formation of high-temperature anhydrous oxysalts (Pekov et al. 2018). However, the very first discoveries of natural oxyarsenates were confined to other mineralization type – the arsenide ores that underwent dry oxidation at high temperatures, the process known in ore mineral processing as pyrolytic oxidation (roasting) (e.g., Dunn and Chamberlain 1997). These assemblages represent, in fact, the combustion products of ores containing nickeline NiAs, skutterudite $(Co,Ni)As_3$, safflorite $CoAs_2$, and rammelsbergite $NiAs_2$. The first described mineral in this family was aerugite $Ni_{8.5}(AsO_4)_2AsO_8$ (Bergemann 1858; Davis et al. 1965; Fleet and Barbier 1989), followed by a discovery of paganoite $NiBiAsO_5$ (Roberts et al. 2001). The origin of these

assemblages, also containing other anhydrous Ni-Co arsenates and bunsenite (natural NiO), was discussed by Kampf et al. (2020).

Taking into account the chemical proximity of arsenic and phosphorus, one could expect that the processes similar to high-temperature roasting of arsenide ores could also occur within natural phosphide assemblages. The combination of factors, which would allow the onset and maintenance of such processes, is quite exotic: it must involve the presence of phosphides (which are very rare in nature), highly oxidative conditions and high temperatures. The synthetic $V^{3+}$ analogue of crocobelonite-2*O* (Boudin et al. 1996) was obtained at temperature 1100 °C - the level that can be used for the estimation of crocobelonite formation conditions. This value looks reasonable as it lies in between the assumed formation temperatures of natural Fe-Ni phosphides – 800–900 °C (Britvin et al. 2020ab, 2021b, 2022a) and the temperatures of at least 1450 °C which took place during solidification of rock-forming mineral assemblages in the Hatrurim Formation (Sharygin et al. 2016). This value is considerably higher than the range of 500-750 °C assumed for the formation of volcanic fumarolic arsenates (Pekov et al. 2018). Such unusual formation environment was realized during the pyrometamorphic processes occurred in the Hatrurim Formation, that resulted in the emergence of a new type of phosphate mineralization (Britvin et al. 2021a), in which crocobelonite represents the first oxyphosphate species.

## Acknowledgements

The authors are thankful to Adam Pieczka and an anonymous referee, as well to the members of CNMNC, International Mineralogical Association, for valuable comments and suggestions. We are indebted to Associate Editor, Fabrizio Nestola, for editorial handling of the manuscript. This study was carried out with the financial support of the Russian Science Foundation, grant 18-17-00079. We thank the Centre for X-ray diffraction studies, Geomodel Resource Centre, and Centre of

315 Microscopy and Microanalysis of St. Petersburg State University for the access to instrumental and
316 computational resources.

317

318 **References**

319 Abzalov, M.Z., Heyden, A., van der, Saymeh, A., and Abuqudaira, M. (2015) Geology and
320 metallogeny of Jordanian uranium deposits. Applied Earth Science, 124, 63–77.
321 Al-Ajarmeh, N., and Khoury, H. (2018) Apatite-rich pyrometamorphic rocks from Suweileh area,
322 Jordan. Arabian Journal of Geoscience, 11, 520.
323 Baur, W.H. (2007) The rutile type and its derivatives. Crystallography Reviews, 13, 65–113.
324 Ben-Avraham, Z., Garfunkel, Z., and Lazar, M. (2008) Geology and evolution of the Southern Dead
325 Sea Fault with emphasis on subsurface structure. Annual Review of Earth and Planetary
326 Sciences, 36, 357–387.
327 Bentor, Y.K., Gross, S., and Heller, L. (1963) Some unusual minerals from "Mottled Zone"
328 complex, Israel. American Mineralogist, 48, 924–930.
329 Bergemann, C. (1858) Ueber einige Nickelerze. Journal für Praktische Chemie, 75, 239–244.
330 Boudin, S., Grandin, A., Borel, M.M., Leclaire, A., and Raveau, B. (1994) A vanadium(III)
331 monophosphate built up from rutile chains: $CdV_2O(PO_4)_2$. Journal of Solid State Chemistry,
332 111, 380–384.
333 Boudin, S., Grandin, A., Leclaire, A., Borel, M.M., and Raveau, B. (1995) $CaV_2O(PO_4)_2$, isotypic
334 with the Cd phase. Acta Crystallographica, C51, 796–798.
335 Boudin, S., Grandin, A., Labbé, Ph., Provost, J., and Raveau, B. (1996) The V(III) monophosphate
336 series $AV_2O(PO_4)_2$ with $A$ = Cd, Ca, Sr: structure and magnetism. Journal of Solid State
337 Chemistry, 127, 325–330.

Breese, N.E., and O'Keefe, M. (1991) Bond-Valence Parameters for Solids. Acta Crystallographica, B47, 192–197.

Britvin, S.N., Murashko, M.N., Vapnik, Ye., Polekhovsky, Yu.S., and Krivovichev, S.V. (2015) Earth's phosphides in Levant and insights into the source of Archaean prebiotc phosphorus. Scientific Reports, 5, 8355.

Britvin, S.N., Murashko, M.N., Vapnik, Ye., Polekhovsky, Yu.S., and Krivovichev, S.V. (2017a) Barringerite $Fe_2P$ from pyrometamorphic rocks of the Hatrurim Formation, Israel. Geology of Ore Deposits, 59, 619–625.

Britvin, S.N., Dolivo-Dobrovolsky, D.V., and Krzhizhanovskaya, M.G. (2017) Software for processing the X-ray powder diffraction data obtained from the curved image plate detector of Rigaku RAXIS Rapid II diffractometer. Zapiski Rossiiskogo Mineralogicheskogo Obshchestva, 146(3), 104–107 (in Russian).

Britvin, S.N., Murashko, M.N., Vapnik, Ye., Polekhovsky, Yu.S., Krivovichev, S.V., Vereshchagin, O.S., Vlasenko, N.S., Shilovskikh, V.V., and Zaitsev, A.N. (2019a) Zuktamrurite, $FeP_2$, a new mineral, the phosphide analogue of löllingite, $FeAs_2$. Physics and Chemistry of Minerals, 46, 361–369.

Britvin, S.N., Vapnik, Ye., Polekhovsky, Yu.S., Krivovichev, S.V., Krzhizhanovskaya, M.G., Gorelova, L.A., Vereshchagin, O.S., Shilovskikh, V.V., and Zaitsev, A.N. (2019b) Murashkoite, FeP, a new terrestrial phosphide from pyrometamorphic rocks of the Hatrurim Formation, Southern Levant. Mineralogy and Petrology, 113, 237–248.

Britvin, S.N., Murashko, M.N., Vapnik, Ye., Polekhovsky, Yu.S., Krivovichev, S.V., Krzhizhanovskaya, M.G., Vereshchagin, O.S., Shilovskikh, V.V., and Vlasenko, N.S. (2020a) Transjordanite, $Ni_2P$, a new terrestrial and meteoritic phosphide, and natural solid solutions barringerite–transjordanite (hexagonal $Fe_2P$–$Ni_2P$). American Mineralogist, 105, 428–436.

Britvin, S.N., Murashko, M.N., Vapnik, Ye., Polekhovsky, Yu.S., Krivovichev, S.V., Vereshchagin, O.S., Shilovskikh, V.V., Vlasenko, N.S., and Krzhizhanovskaya, M.G. (2020b) Halamishite, $Ni_5P_4$, a new terrestrial phosphide in the Ni–P system. Physics and Chemistry of Minerals, 2020, 3.

Britvin, S.N., Murashko, M.N., Vapnik, Ye., Polekhovsky, Yu.S., Krivovichev, S.V., Vereshchagin, O.S., Shilovskikh, V.V., and Krzhizhanovskaya, M.G. (2020c) Negevite, the pyrite-type $NiP_2$, a new terrestrial phosphide. American Mineralogist, 105, 422–427.

Britvin, S.N., Murashko, M.N., Vapnik, Ye., Vlasenko, N.S., Krzhizhanovskaya, M.G., Vereshchagin, O.S., Bocharov, V.N., and Lozhkin, M.S. (2021a) Cyclophosphates, a new class of native phosphorus compounds, and some insights into prebiotic phosphorylation on early Earth. Geology, 49, 382–386.

Britvin, S.N., Vereshchagin, O.S., Shilovskikh, V.V., Krzhizhanovskaya, M.G., Gorelova, L.A., Vlasenko, N.S., Pakhomova, A.S., Zaitsev, A.N., Zolotarev, A.A., Bykov, M., Lozhkin, M.S., and Nestola, F. (2021b) Discovery of terrestrial allabogdanite $(Fe,Ni)_2P$, and the effect of Ni and Mo substitution on the barringerite-allabogdanite high-pressure transition. *American Mineralogist*, **106**, 944–952.

Britvin, S.N., Murashko, M.N., Krzhizhanovskaya, M.G., Vereshchagin, O.S., Vapnik, Ye., Shilovskikh, V.V., Lozhkin, M.S., and Obolonskaya, E.V. (2022a) Nazarovite, $Ni_{12}P_5$, a new terrestrial and meteoritic mineral structurally related to nickelphosphide, $Ni_3P$. American Mineralogist, doi:10.2138/am-2022-8219.

Britvin, S.N., Murashko, M.N., Vereshchagin, O.S., Vapnik, Ye., Shilovskikh, V.V., Vlasenko, N.S., and Permyakov, V.V. (2022b) Expanding the speciation of terrestrial molybdenum: discovery of polekhovskyite, $MoNiP_2$, and insights into the sources of Mo-phosphides in the Dead Sea Transform area, *American Mineralogist*, doi:10.2138/am-2022-8261.

Britvin, S.N., Vlasenko, N.S., Aslandukov, A., Aslandukova, A., Dubrovinsky, L., Gorelova, L.A., Krzhizhanovskaya, M.G., Vereshchagin, O.S., Bocharov, V.N., Shelukhina, Yu.S., Lozhkin, M.S., Zaitsev, A.N., and Nestola, F. (2022c) Natural cubic perovskite, $Ca(Ti,Si,Cr)O_{3-\delta}$, a versatile potential host for rock-forming and less common elements up to Earth's mantle pressure. American Mineralogist, doi: 10.2138/am-2022-8186

Burg, A., Starinsky, A., Bartov, Y., and Kolodny, Y. (1992) Geology of the Hatrurim Formation ("Mottled Zone") in the Hatrurim basin. Israel Journal of Earth Sciences, 40, 107–124.

Cipriani, C., Mellini, M., Pratesi, G., and Viti, C. (1997) Rodolicoite and grattarolaite, two new phosphate minerals from Santa Barbara Mine, Italy. European Journal of Mineralogy, 9, 1101–1106.

Davis, R.J., Hey, M.H., and Kingsbury, A.W.G. (1965) Xanthiosite and aerugite. Mineralogical Magazine, 35, 72–83.

Dolomanov, O.V., Bourhis, L.J., Gildea, R.J., Howard, J.A., and Puschmann, H. (2009) OLEX2: a complete structure solution, refinement and analysis program, Journal of Applied Crystallography, 42, 339–341.

Dunn, J.G., and Chamberlain, A.C. (1997) The recovery of gold from refractory arsenopyrite concentrates by pyrolysis-oxidation. Minerals Engineering, 10, 919–928.

Eckhardt, E.J., and Heimbach, W. (1963) Ein natürliches Vorkommen von $CaCrO_4$ (Chromatit). Naturwissenschaften, 50, 612.

Fleurance, S., Cuney, M., Malartre, M., and Reyx, J. (2013) Origin of the extreme polymetallic enrichment (Cd, Cr, Mo, Ni, U, V, Zn) of the Late Cretaceous–Early Tertiary Belqa Group, central Jordan. Palaeogeography, Palaeoclimatology, Palaeoecology, 369, 201–219.

Fleet, M.E., and Barbier, J. (1989) Structure of aerugite ($Ni_{8.5}As_3O_{16}$) and interrelated arsenate and germanate structural series. Acta Crystallographica, B45, 201–205.

Gaines, R.V., Skinner, H.C.W., Foord, E.E., Mason, B., and Rosenzweig, A. (1997) Dana's New Mineralogy: The system of mineralogy of James Dwight Dana and Edward Salisbury Dana, 8th ed. Wiley, New York.

Galuskin, E.V., Galuskina, I.O., Kusz, J. Armbruster, T., Marzec, K.M., Dzierżanowski, P., and Murashko, M. (2014) Vapnikite $Ca_3UO_6$ – a new double-perovskite mineral from pyrometamorphic larnite rocks of the Jabel Harmun, Palestinian Autonomy, Israel. Mineralogical Magazine, 78, 571–581.

Galuskina, I.O., Galuskin, E.V., Prusik, K., Vapnik, Y., Juroszek, R., Jeżak, L., and Murashko, M. (2017) Dzierżanowskite, $CaCu_2S_2$ – A new natural thiocuprate from Jabel Harmun, Judean Desert, Palestine Autonomy, Israel. Mineralogical Magazine, 81, 777–789.

Galuskina, I., Galuskin, E., Vapnik, Y., Zeliński, G., and Prusik, K. (2021a) Priscillagrewite-(Y), $(Ca_2Y)Zr_2Al_3O_{12}$: A new garnet of the bitikleite group from the Daba-Siwaqa area, the Hatrurim Complex, Jordan. American Mineralogist, 106, 641–649.

Galuskina, I.O., Stachowicz, M., Woźniak, K., Vapnik, Y., and Galuskin, E. (2021b) Mcconnellite, $CuCrO_2$ and ellinaite, $CaCr_2O_4$, from varicoloured spurrite marble of the Daba-Siwaqa area, Hatrurim Complex, Jordan. Mineralogical Magazine 85, 387–397.

Garfunkel, Z., and Ben-Avraham, Z. (1996) The structure of the Dead Sea basin. Tectonophysics, 266, 155–176.

Gross, S. (1977) The mineralogy of the Hatrurim Formation, Israel. Geological Survey of Israel Bulletin, 70, 1–80.

Gross, S. (1980) Bentorite. A new mineral from the Hatrurim Area, west of the Dead Sea, Israel. Israel Journal of Earth Sciences, 29, 81–84.

Grossman, J.N., Alexander, C.M.O'D., Wang, J., and Brearley, A.J. (2000) Bleached chondrules: Evidence for widespread aqueous processes on the parent asteroids of ordinary chondrites. Meteoritics and Planetary Science, 35, 467–486.

Gur, D., Steinitz, G., Kolodny, Y., Starinsky, A., and McWilliams, M. (1995) $^{40}Ar/^{39}Ar$ dating of combustion metamorphism ("Mottled Zone", Israel). Chemical Geology, 122, 171–184.

Hauff, P.L., Foord, E.E., Rosenblum, S., and Hakki, W. (1983) Hashemite, $Ba(Cr,S)O_4$, a new mineral from Jordan. American Mineralogist, 68, 1223–1225.

Ito, T. (1950) X-ray studies on polymorphism, p. 1-6. Maruzen, Tokyo.

Juroszek, R., Krüger, B., Galuskina, I., Krüger, H., Vapnik, Ye., and Galuskin, E. (2020) Siwaqaite, $Ca_6Al_2(CrO_4)_3(OH)_{12}\cdot 26H_2O$, a new mineral of the ettringite group from the pyrometamorphic Daba-Siwaqa complex, Jordan. American Mineralogist, 105, 409–421.

Kampf, A.R., Nash, B.P., Plášil, J., Smith, J.B., and Feinglos, M.N. (2020) Niasite and johanngeorgenstadtite, $Ni^{2+}_{4.5}(AsO_4)_3$ dimorphs from Johanngeorgenstadt, Germany. European Journal of Mineralogy, 32, 373–385.

Keller, P., Fontan, F., Velasco-Roldan, F., and Melgarejo i Draper, J.C. (1997) Staněkite, $Fe^{3+}(Mn,Fe^{2+},Mg)(PO_4)O$: a new phosphate mineral in pegmatites at Karibib (Namibia) and French Pyrenees (France). European Journal of Mineralogy, 9, 475–482.

Keller, P., Fontan, F., Roldan, F.V., and de Parseval, P. (2007) Joosteite, $Mn^{2+}(Mn^{3+},Fe^{3+})(PO_4)O$: a new phosphate mineral from the Helikon II Mine, Karibib, Namibia. Neues Jahrbuch für Mineralogie – Abhandlungen, 183, 197–201.

Khoury, H.N. (2019) Industrial rocks and minerals of Jordan: a review. Arabian Journal of Geosciences, 12, 619.

Khoury, H.N. (2020) High- and low-temperature mineral phases from the pyrometamorphic rocks, Jordan. Arabian Journal of Geosciences, 13, 734.

Khoury, H., and Nassir, S. (1982a) A discussion on the origin of Daba-Siwaqa marble. Dirasat, 9, 55–56.

Khoury, H., and Nassir, S. (1982b) High temperature mineralization in Maqarin area, North Jordan. Neues Jahrbuch für Mineralogie (Abhandlungen), 144, 197–213.

Kolodny, Y., and Gross, S. (1974) Thermal metamorphism by combustion of organic matter: Isotopic and petrological evidence. The Journal of Geology, 82, 489–506.

Kolodny, Y., Burg, A., Geller, Y.I., Halicz, L., and Zakon, Y. (2014) Veins in the combusted metamorphic rocks, Israel; weathering or a retrograde event? Chemical Geology, 385, 140–155.

Krivovichev, S.V. (2008) Structural Crystallography of Inorganic Oxysalts. Oxford University Press, U.K.

Krivovichev, V.G. (2021) Mineral Species. St. Petersburg University Press, St. Petersburg (in Russian).

Kurat, G. (1969) The formation of chondrules and chondrites and some observations on chondrules from the Tieschitz meteorite. In Meteorite Research (ed. P. Millman), pp. 185-190. D. Reidel Publ. Co., Dordrecht, the Netherlands.

Mandarino, J.A. (1976) The Gladstone-Dale relationship. Part I: Derivation of new constants. Canadian Mineralogist, 14, 498–502.

Mills, S.J., Kampf, A.R., Poirier, G., Raudsepp, M., and Steele, I.M. (2010) Auriacusite, $Fe^{3+}Cu^{2+}AsO_4O$, the first $M^{3+}$ member of the olivenite group, from the Black Pine mine, Montana, USA. Mineralogy and Petrology, 99, 113–120.

Moore, P.B., and Araki, T. (1978) Angelellite, $Fe_4^{3+}O_3(As^{5+}O_4)_2$: a novel cubic close-packed oxide structure. Neues Jahrbuch für Mineralogie, Abhandlungen, 132, 91–100.

Nakamoto K. (2008) Infrared and Raman Spectra of Inorganic and Coordination Compounds, Theory and Applications in Inorganic Chemistry. John Wiley and Sons, New York.

Nakamoto K. (2009) Infrared and Raman Spectra of Inorganic and Coordination Compounds, Part B, Applications in Coordination, Organometallic, and Bioinorganic Chemistry. John Wiley and Sons, Hoboken.

Nathan, Y., Shiloni, Y., Roded, R., Gal, I., and Deutsch, Y. (1979) The geochemistry of the northern Negev phosphorites (Southern Israel). Geological Survey of Israel Bulletin, 73, 41 p.

Nickel, E.H., and Grice, J. (1998) The IMA Commission on New Minerals and Mineral Names: Procedures and guidelines on mineral nomenclature. The Canadian Mineralogist, 36, 913–926.

Novikov, I., Vapnik, Ye., and Safonova, I. (2013) Mud volcano origin of the Mottled Zone, Southern Levant. Geoscience Frontiers, 4, 597–619.

Pekov, I.V., Koshlyakova, N.N., Zubkova, N.V., Lykova, I.S., Britvin, S.N., Yapaskurt, V.O., Agakhanov, A.A., Shchipalkina, N.V., Turchkova, A.G., and Sidorov, E.G. (2018) Fumarolic arsenates - a special type of arsenic mineralization. European Journal of Mineralogy, 30, 305–322.

Pekov, I.V., Zubkova, N.V., Agakhanov, A.A., Ksenofontov, D.A., Pautov, L.A., Sidorov, E.G., Britvin, S.N., Vigasina, M.F., and Pushcharovsky, D.Y. (2019a) New arsenate minerals from the Arsenatnaya fumarole, Tolbachik volcano, Kamchatka, Russia. X. Edtollite, $K_2NaCu_5Fe^{3+}O_2(AsO_4)_4$, and alumoedtollite, $K_2NaCu_5AlO_2(AsO_4)_4$. Mineralogical Magazine, 83, 485–495.

Pekov, I.V., Zubkova, N.V., Agakhanov, A.A., Belakovskiy, D.I., Vigasina, M.F., Yapaskurt, V.O., Sidorov, R.G., Britvin, S.N., and Pushcharovsky, D.Y. (2019b) New arsenate minerals from the Arsenatnaya fumarole, Tolbachik volcano, Kamchatka, Russia. IX. Arsenatrotitanite, $NaTiO(AsO_4)$. Mineralogical Magazine, 83, 453–458.

Pekov, I.V., Britvin, S.N., Yapaskurt, V.O., Krivovichev, S.V., Vigasina, M.F., and Sidorov, E.G. (2021a) Vasilseverginite, $Cu_9O_4(AsO_4)_2(SO_4)_2$, a new fumarolic mineral with a hybrid structure containing novel anion-centered tetrahedral structural units. American Mineralogist, 106, 633–640.

Pekov, I.V., Zubkova, N.V., Agakhanov, A.A., Yapaskurt, V.O., Belakovskiy, D.I., Vigasina, M.F., Britvin, S.N., Turchkova, A.G., Sidorov, E.G., and Pushcharovsky, D.Yu. (2021b) New arsenate minerals from the Arsenatnaya fumarole, Tolbachik volcano, Kamchatka, Russia. XVI. Yurgensonite, $K_2SnTiO_2(AsO_4)_2$, the first natural tin arsenate, and the katiarsite–yurgensonite isomorphous series. Mineralogical Magazine, 85, 698–707.

Picard, L. Geological researches in the Judean Desert. Jerusalem, Goldberg Press, 1931, 108 p.

Rigaku Oxford Diffraction (2021) CrysAlisPro, data collection and data reduction GUI, Rigaku Corporation, Tokyo, Japan.

Roberts, A.C., Burns, P.C., Gault, R.A., Criddle, A.J., Feinglos, M.N., and Stirling, J.A.R. (2001) Paganoite, $NiBiAsO_5$, a new mineral from Johanngeorgenstadt, Saxony, Germany: description and crystal structure. European Journal of Mineralogy, 13, 167–175.

Shablinskii, A.P., Filatov, S.K., Vergasova, L.P., Avdontseva, E.Y., and Moskaleva, S.V. (2018) Wrightite, $K_2Al_2O(AsO_4)_2$, a new oxo-orthoarsenate from the Second scoria cone, Northern Breakthrough, Great Fissure eruption, Tolbachik volcano, Kamchatka peninsula, Russia. Mineralogical Magazine, 82, 1243–1251.

Sharygin, V.V., Lazic, B., Armbruster, T.M., Murashko, M.N., Wirth, R., Galuskina, I.O., Galuskin, E.V., Vapnik, Y., Britvin, S.N., and Logvinova, A.M. (2013): Shulamitite, $Ca_3TiFe^{3+}AlO_8$ - a new perovskite-related mineral from Hatrurim Basin, Israel. European Journal of Mineralogy 25, 97–111.

Sharygin, V.V., Vapnik, Y., Sokol, E.V., Kamenetsky, V.S., and Shagam, R. (2016) Melt inclusions in minerals of schorlomite-rich veins of the Hatrurim Basin, Israel: Composition and homogenization temperatures. In P. Ni, Z. Li, Eds., Proceedings of the ACROFI I, p. 189–192, Elsevier, The Netherlands.

Sharygin, V.V., Britvin, S.N., Kaminsky, F.V., Wirth, R., Nigmatulina, E.N., Yakovlev, G.A., Novoselov, K.A., and Murashko, M.N. (2021): Ellinaite, $CaCr_2O_4$, a new natural post-spinel oxide from Hatrurim Basin, Israel, and Juína kimberlite field, Brazil. European Journal of Mineralogy, 33, 727–742.

Sheldrick, G.M. (2015) Crystal structure refinement with SHELXL. Acta Crystallographica, C71, 3–8.

Sokol, E.V., Kokh, S.N., Vapnik, Y., Thiéry, V., and Korzhova, S.A. (2014) Natural analogs of belite sulfoaluminate cement clinkers from Negev Desert, Israel. American Mineralogist, 99, 1471–1487.

Sokol, E.V., Kokh, S.N., Sharygin, V.V., Danilovsky, V.A., Seryotkin, Yu.V., Liferovich, R., Deviatiiarova, A.S., Nigmatulina, E.N., and Karmanov, N.S. (2019) Mineralogical diversity of $Ca_2SiO_4$-bearing combustion metamorphic rocks in the Hatrurim Basin: implications for storage and partitioning of elements in oil shale clinkering. Minerals, 9, 465.

Strunz, H., and Nickel, E.H. (2001) Strunz Mineralogical Tables, 9th edition, E. Schweizerbart Verlag, Stuttgart, 870 p.

Vapnik, Ye., Sharygin, V., Sokol, E., and Shagam, R. (2007) Paralavas in a combustion metamorphic complex, Hatrurim Basin, Israel. GSA Reviews in Engineering Geology, 18, 33–153.

548 Vergasova, L.P., Filatov, S.K., Gorskaya, M.G., Molchanov, A.A., Krivovichev, S.V., and Ananiev,
549 V.V. (2000) Urusovite, Cu[$AlAsO_5$], a new mineral from the Tolbachik volcano, Kamchatka,
550 Russia. European Journal of Mineralogy, 12, 1041–1044.
551 Weber, D., and Bischoff, A. (1994) Grossite, $CaAl_4O_7$ - a rare phase in terrestrial rocks and
552 meteorites. European Journal of Mineralogy, 6, 591–594.
553 Yau, Y.C., and Peacor, D.R. (1986) Jerrygibbsite-leucophoenicite mixed layering and general
554 relations between the humite and leucophoenicite families. American Mineralogist, 71, 985–
555 988.
556
557

## List of figure captions

**Figure 1.** The territory of the Middle East. The fields of the pyrometamorphic rocks belonging to the Hatrurim Formation (the Mottled Zone) are indicated by red areas and circles, with two localities of crocobelonite (the Hatrurim Basin in Israel and Daba-Siwaqa complex in Jordan). Adapted from Britvin et al. (2021a).

**Figure 2.** The phosphorite quarry in the Daba-Siwaqa complex – the type locality for crocobelonite-2*O*. (a) The overview of the outcrop containing crocobelonite. (b) The black xenolith of partially assimilated phosphorite within the olive-coloured hornfel. (3) The veinlets of bluish-green fluorapatite in a block of varicolored hornfel.

**Figure 3.** Crocobelonite in phosphate-phosphide assemblages from the phosphorite quarry at the Daba-Siwaqa complex, Jordan (the type locality). (a) The overview of a typical sample of phosphate-bearing paralava. (b) Diopside crystals filling up the paralava. Thin section, transmitted light, XPL. (c) Diopside clumps within the same paralava sample. Thin section, PPL. (d) Cross-section of a typical phosphate-phosphide bearing bubble within paralava. Red areas are crocobelonite aggregates. Thin section, scattered light. (e) Chondrule-like segregations of calcium silicophosphates (indicated as Ch within the bubble in Fig. 3d). Thin section, transmitted light (f) The detail of crocobelonite-bearing area shown in Fig. 3d. Abbreviations: Di – diopside, Ph – phosphides, Hem – hematite, Ch – hondrules, Ccb – crocobelonite.

**Figure 4.** Crocobelonite crystals in the paralava microcavities. (a) Aggregates of prismatic crystals intergrown with hematite (black) and diopside (white). (b) Prismatic crocobelonite crystal. Phosphorite quarry, Daba-Siwaqa complex, Jordan.

**Figure 5**. Two polymorphic modifications of crocobelonite in a complex phosphate assemblage. Nahal Halamish, Hatrurim Basin, Negev Desert, Israel. (a) Phosphate-bearing nest; photomicrograph of a polished section in scattered light. (b) The same field in reflected light. (c) SEM BSE image of the area. The highlighted rectangle outlines the area subjected to EBSD mapping. (d) EBSD crocobelonite phase map of an area highlighted in (c), superimposed onto BSE image. The red patches denote clinocrocobelonite; the yellow ones correspond to crocobelonite. (e) EBSD IPF (inverse pole figure) map. The different colours correspond to different orientations of crocobelonite crystals. Legend: M –crocobelonite-1*M*; O – crocobelonite-2*O*; Ald – unnamed alluaudite-group phosphate; Hm – hematite; Glass – Ca-Si-P-O glass.

**Figure 6.** Rietveld refinement plot for crocobelonite-2*O*.

**Figure 7.** Crystal structure of crocobelonite, in projection that emphasizes structural similarity of both polymorphs. The unit-cell axes of crocobelonite-2*O* are shown in blue; the axes of crocobelonite-1*M* are black. A three-dimensional framework composed of two types of structural subunits. The first one is represented by the infinite "rutile-like" chains (rods) of edge-sharing $Fe(1)O_6$ octahedra, propagating along the *b*-axis in both polymorphs. The second type of subunit is comprised by the infinite chains $[Fe(2)PO_8]$, also running along the *b*-axis and composed of corner-sharing $Fe(2)O_6$ octahedra and $PO_4$ tetrahedra. The rods are connected into a framework via the

603 inter-rod [$FeO_6$] octahedra and [$PO_4$] tetrahedra together with [$CaO_7$] polyhedra (the latter are not
604 shown for clarity). Legend: [$FeO_6$] – red; [$PO_4$] – yellow.
605
606 **Figure 8.** Fragment of crocobelonite structure showing the linkages between tetrahedral [$PO_4$] and
607 octahedral [$FeO_6$].
608
609 **Figure 9.** Structural relationship between crocobelonite polymorphs. Projections onto {010}. (a)
610 Crocobelonite-1*M*. The unit cell is highlighted by gray colour. (b) Crocobelonite-2*O*. The unit cell is
611 highlighted by blue colour. Stacking of building sub-layers in crocobelonite-2*O* can be expressed as
612 the "unit-cell twinning" of crocobelonite-1*M* cells, where the "twinned" 1*M* cells are related by the
613 mirror plane {100} and half-cell translation along the *c*-axis (in orthorhombic setting). Legend:
614 [$FeO_6$] – red; [$PO_4$] – yellow.
615
616 **Figure 10.** The mid-angle ranges of powder X-ray diffraction patterns of crocobelonite-1*M* and
617 crocobelonite-2*O*. Note the substantial differences in the patterns due to the differences in the crystal
618 structures and lattice geometries.
619
620 **Figure 11.** Raman spectra of crocobelonite polymorphs. (a) The fingerprint region. (b) The high-
621 frequency part beyond 1500 $cm^{-1}$. The absence of vibrations in the OH-stretching region indicates
622 for the lack of hydroxyl water.
623
624

625 **Table 1**. Optical properties of crocobelonite

626

| | Crocobelonite-2*O* | Crocobelonite-1*M* |
|---|---|---|
| Colour | brownish-orange | |
| Pleochroism | very strong; *X* and *Y* – pale-yellow, *Z* – deep brownish-orange | |
| α | 1.885(5) | 1.835(5) |
| β | 1.885(5) | 1.935(5) |
| γ | 1.950(5) | 1.955(5) |
| 2V (°) | ~ (+)10 (meas.) | (–)44 (calc.) |
| Compatibility [a] | –0.041 (good) | –0.031 (excellent) |

627

628 [a] The Gladstone-Dale compatibility index (Mandarino 1976).

629

630

631

632

633 **Table 2**. Chemical composition of crocobelonite

634

| | Crocobelonite-2*O* [a] | | | Crocobelonite-1*M* [b] | | |
|---|---|---|---|---|---|---|
| | Mean | Range ($n$ = 7) | 2σ | Mean | Range ($n$ = 8) | 2σ |
| CaO | 16.03 | 15.80 – 16.26 | 0.18 | 15.56 | 15.42 – 15.78 | 0.13 |
| MgO | 0.56 | 0.40 – 0.77 | 0.13 | 0.16 | 0.00 – 0.31 | 0.10 |
| NiO | | b.d.l. [c] | | 0.78 | 0.50 – 0.97 | 0.17 |
| $Fe_2O_3$ | 43.37 | 43.10 – 43.79 | 0.25 | 41.28 | 40.52 – 42.03 | 0.56 |
| $Al_2O_3$ | 0.33 | 0.24 – 0.44 | 0.08 | 0.45 | 0.34 – 0.56 | 0.07 |
| $V_2O_3$ | | b.d.l. | | 0.42 | 0.25 – 0.51 | 0.09 |
| $Cr_2O_3$ | | b.d.l. | | 0.23 | 0.00 – 0.32 | 0.10 |
| $TiO_2$ | | b.d.l. | | 0.79 | 0.49 – 1.18 | 0.24 |
| $SiO_2$ | 0.32 | 0.26 – 0.38 | 0.04 | | b.d.l. | |
| $P_2O_5$ | 39.45 | 38.82 – 39.80 | 0.39 | 39.94 | 39.71 – 40.13 | 0.15 |
| Total | 100.06 | | | 99.61 | | |

635

636 [a] Holotype material: phosphorite quarry, Daba-Siwaqa complex, Jizah District, Amman
637 Governorate, Jordan. [b] Holotype material: Halamish Wadi, Hatrurim Basin, Negev Desert,
638 Israel. [c] b.d.l. – below detection limit.

639

640

This is the peer-reviewed, final accepted version for American Mineralogist, published by the Mineralogical Society of America.
The published version is subject to change. Cite as Authors (Year) Title. American Mineralogist, in press.
DOI: https://doi.org/10.2138/am-2022-8757. http://www.minsocam.org/

641

642 **Table 3**. Crystallographic data for crocobelonite polymorphs and synthetic $CaV_2O(PO_4)_2$

| | Crocobelonite-2*O* SCXRD | Crocobelonite-2*O* Rietveld refinement | Synthetic [a] $CaV_2O(PO_4)_2$ | Crocobelonite-1*M* SCXRD |
|---|---|---|---|---|
| Chemical formula | $CaFe^{3+}_2(PO_4)_2O$ | $CaFe^{3+}_2(PO_4)_2O$ | $CaV^{3+}_2(PO_4)_2O$ | $CaFe^{3+}_2(PO_4)_2O$ |
| Structure type | $CdV^{3+}_2(PO_4)_2O$ [b] | $CdV^{3+}_2(PO_4)_2O$ [b] | $CdV^{3+}_2(PO_4)_2O$ [b] | New |
| Crystal system | Orthorhombic | Orthorhombic | Orthorhombic | Monoclinic |
| Space group | *Pnma* | *Pnma* | *Pnma* | $P2_1/m$ |
| *a* (Å) | 14.2392(8) | 14.2757(1) | 14.192(1) | 7.2447(2) [~ *c*(2*O*)] |
| *b* (Å) | 6.3632(3) | 6.3832(1) | 6.424(1) | 6.3832(1) |
| *c* (Å) | 7.2880(4) [~ *a*(1*M*)] | 7.3169(1) [~ *a*(1*M*)] | 7.317(1) | 7.3993(2) |
| β (°) | | | | 106.401(2) |
| *Z* | 4 | 4 | 4 | 2 |
| *V*/*Z* (Å$^3$) | 160.09 | 166.69 | 166.77 | 164.13 |
| $D_x$ (g cm$^{-3}$) [c] | 3.60 | 3.56 | 3.46 | 3.62 |

643

644 [a] Boudin et al. (1995). [b] Boudin et al. (1994). [c] Densities calculated for ideal formulae.

645

This is the peer-reviewed, final accepted version for American Mineralogist, published by the Mineralogical Society of America.
The published version is subject to change. Cite as Authors (Year) Title. American Mineralogist, in press.
DOI: https://doi.org/10.2138/am-2022-8757. http://www.minsocam.org/

646 **Table 4**. Selected bond lengths (Å) and bond-valence sums (BVS, v.u.) for crocobelonite [a]

647

| Bond | Crocobelonite-2*O* SCXRD | Crocobelonite-2*O* Rietveld refinement | Crocobelonite-1*M* SCXRD |
|---|---|---|---|
| Ca–O1 | 2.416(5) ×2 | 2.393(2) ×2 | 2.4259(14) ×2 |
| Ca–O2 | 2.491(8) | 2.475(3) | 2.433(2) |
| Ca–O4 | 2.431(8) | 2.444(3) | 2.479(2) |
| Ca–O5 | 2.899(8) | 2.918(4) | 2.711(2) |
| Ca–O7 | 2.331(5) ×2 | 2.339(1) ×2 | 2.3452(15) ×2 |
| < Ca–O> | 2.474 | 2.472 | 2.452 |
| BVS | 1.95 | 1.97 | 1.97 |
| | | | |
| Fe1–O1 | 1.993(5) ×2 | 2.033(2) ×2 | 2.0007(14) |
| Fe1–O2 | 2.238(8) | 2.226(3) | 2.262(2) |
| Fe1–O3 | 1.904(8) | 1.861(4) | 1.894(2) |
| Fe1–O4 | 2.068(7) | 2.114(3) | 2.056(2) |
| Fe1–O5 | 1.890(7) | 1.870(4) | 1.887(2) |
| < Fe1–O> | 2.014 | 2.023 | 2.017 |
| BVS | 3.15 | 3.12 | 3.15 |
| | | | |
| Fe2–O5 | 1.991(4) ×2 | 2.018(2) ×2 | 2.0341(12) |
| Fe2–O6 | 2.058(5) ×2 | 2.067(2) ×2 | 2.0525(12) |
| Fe2–O7 | 2.018(5) ×2 | 2.009(2) ×2 | 2.0233(13) |
| < Fe2–O> | 2.022 | 2.031 | 2.037 |
| BVS | 2.95 | 2.88 | 2.83 |
| | | | |
| P1–O2 | 1.538(9) | 1.558(3) | 1.531(2) |
| P1–O4 | 1.536(8) | 1.535(3) | 1.555(2) |
| P1–O7 | 1.534(5) ×2 | 1.543(1) ×2 | 1.5399(14) ×2 |
| < P1–O> | 1.536 | 1.545 | 1.541 |
| BVS | 4.81 | 4.70 | 4.74 |
| | | | |
| P2–O1 | 1.525(5) ×2 | 1.526(2) ×2 | 1.5290(14) ×2 |
| P2–O3 | 1.476(8) | 1.547(4) | 1.496(2) |
| P2–O6 | 1.556(8) | 1.564(4) | 1.559(2) |
| < P2–O> | 1.521 | 1.541 | 1.528 |
| BVS | 5.03 | 4.75 | 4.92 |

648
649 [a] Site labelling corresponds to synthetic $CaV_2(PO_4)_2O$ (Boudin et al. 1995). Bond-valence parameters
650 were taken from Brese and O'Keefe (1991), assuming that Fe sites are populated with $Fe^{3+}$.
651
652

653 **Table 5**. X-ray powder diffraction data (*d* in Å) for crocobelonite-2*O*

| $I_{meas}$ | $d_{meas}$ | $I_{calc}$ | $d_{calc}$ | *hkl* | $I_{meas}$ | $d_{meas}$ | $I_{calc}$ | $d_{calc}$ | *hkl* |
|---|---|---|---|---|---|---|---|---|---|
| 5 | 7.17 | 4 | 7.14 | 200 | 4 | 1.717 | 1 | 1.719 | 810 |
| 16 | 6.54 | 16 | 6.51 | 101 | | | 1 | 1.716 | 712 |
| 26 | 5.12 | 28 | 5.11 | 201 | | | 3 | 1.716 | 332 |
| 3 | 4.824 | 3 | 4.811 | 011 | 5 | 1.703 | 1 | 1.703 | 603 |
| 3 | 4.567 | 3 | 4.558 | 111 | | | 6 | 1.703 | 423 |
| 7 | 3.997 | 4 | 3.989 | 301 | 5 | 1.673 | 6 | 1.673 | 721 |
| | | 4 | 3.989 | 211 | 2 | 1.662 | 2 | 1.662 | 531 |
| 8 | 3.664 | 10 | 3.658 | 002 | 2 | 1.646 | 3 | 1.646 | 613 |
| | | 2 | 3.569 | 400 | 4 | 1.628 | 5 | 1.628 | 404 |
| 100 | 3.549 | 100 | 3.544 | 102 | 10 | 1.604 | 13 | 1.603 | 523 |
| 7 | 3.259 | 7 | 3.256 | 311 | 9 | 1.596 | 10 | 1.596 | 040 |
| 50 | 3.200 | 27 | 3.208 | 401 | 5 | 1.587 | 5 | 1.587 | 024 |
| | | 37 | 3.192 | 020 | | | 2 | 1.586 | 630 |
| 2 | 3.103 | 2 | 3.098 | 112 | 1 | 1.565 | 1 | 1.564 | 703 |
| 19 | 2.912 | 14 | 2.914 | 220 | 1 | 1.557 | 1 | 1.558 | 820 |
| | | 9 | 2.900 | 302 | 1 | 1.549 | 1 | 1.550 | 901 |
| 40 | 2.869 | 14 | 2.866 | 411 | 1 | 1.504 | 2 | 1.503 | 623 |
| | | 30 | 2.866 | 121 | 4 | 1.4550 | 3 | 1.455 | 142 |
| 9 | 2.709 | 8 | 2.707 | 221 | 2 | 1.431 | 1 | 1.433 | 822 |
| 21 | 2.662 | 24 | 2.660 | 501 | | | 2 | 1.429 | 441 |
| 6 | 2.556 | 7 | 2.555 | 402 | 3 | 1.419 | 4 | 1.419 | 912 |
| 16 | 2.493 | 18 | 2.492 | 321 | 3 | 1.397 | 3 | 1.398 | 533 |
| 7 | 2.457 | 7 | 2.455 | 511 | | | 2 | 1.393 | 10.1.0 |
| 8 | 2.406 | 5 | 2.405 | 022 | 4 | 1.368 | 3 | 1.368 | 541 |
| | | 4 | 2.404 | 103 | | | 2 | 1.366 | 732 |
| 10 | 2.376 | 3 | 2.379 | 420 | 2 | 1.330 | 1 | 1.3296 | 633 |
| | | 8 | 2.372 | 122 | | | 1 | 1.3295 | 143 |
| 6 | 2.282 | 6 | 2.279 | 222 | 2 | 1.3244 | 2 | 1.3241 | 922 |
| | | 1 | 2.278 | 013 | 1 | 1.2516 | 2 | 1.2507 | 443 |
| 20 | 2.264 | 3 | 2.263 | 601 | 3 | 1.2019 | 3 | 1.2012 | 932 |
| | | 19 | 2.262 | 421 | 2 | 1.1858 | 1 | 1.1858 | 244 |
| 4 | 2.173 | 4 | 2.170 | 213 | | | 2 | 1.1855 | 10.3.0 |
| 2 | 2.055 | 2 | 2.055 | 313 | 1 | 1.1353 | 1 | 1.1356 | 126 |
| 6 | 2.040 | 6 | 2.039 | 230 | 1 | 1.1087 | 1 | 1.1083 | 10.1.4 |
| 4 | 2.014 | 5 | 2.014 | 403 | 1 | 1.0638 | 1 | 1.0639 | 060 |
| 3 | 1.995 | 3 | 1.994 | 602 | 1 | 1.0605 | 1 | 1.0604 | 11.3.2 |
| 5 | 1.921 | 3 | 1.920 | 413 | 1 | 1.0516 | 1 | 1.0519 | 345 |
| | | 2 | 1.920 | 123 | | | 1 | 1.0518 | 13.0.2 |
| 7 | 1.908 | 6 | 1.908 | 620 | | | 1 | 1.0516 | 553 |
| 2 | 1.855 | 2 | 1.854 | 503 | 1 | 1.0190 | 1 | 1.0195 | 925 |
| 2 | 1.845 | 3 | 1.846 | 621 | | | 2 | 1.0189 | 162 |
| 5 | 1.829 | 5 | 1.829 | 004 | 1 | 1.0092 | 1 | 1.0098 | 461 |
| 3 | 1.795 | 4 | 1.795 | 323 | 1 | 1.0092 | 1 | 1.0087 | 11.3.3 |
| 8 | 1.783 | 3 | 1.784 | 800 | 1 | 0.9973 | 1 | 0.9973 | 12.0.4 |
| | | 7 | 1.781 | 513 | 1 | 0.9973 | 1 | 0.9972 | 844 |
| 3 | 1.773 | 3 | 1.773 | 431 | 1 | 0.9946 | 2 | 0.9948 | 10.3.4 |
| | | 2 | 1.772 | 204 | | | | | |

654

655

This is the peer-reviewed, final accepted version for American Mineralogist, published by the Mineralogical Society of America.
The published version is subject to change. Cite as Authors (Year) Title. American Mineralogist, in press.
DOI: https://doi.org/10.2138/am-2022-8757. http://www.minsocam.org/

656

657 **Table 6**. X-ray powder diffraction data (*d* in Å) for crocobelonite-1*M*

| $I_{meas}$ | $d_{meas}$ | $I_{calc}$ | $d_{calc}$ | *hkl* | $I_{meas}$ | $d_{meas}$ | $I_{calc}$ | $d_{calc}$ | *hkl* |
|---|---|---|---|---|---|---|---|---|---|
| 5 | 7.13 | 6 | 7.10 | 001 | 3 | 1.9528 | 5 | 1.9540 | –303 |
| 17 | 6.98 | 25 | 6.95 | 100 | 1 | 1.9212 | 1 | 1.9249 | –321 |
| 6 | 4.72 | >1 | 4.75 | 011 | | | 1 | 1.9147 | 131 |
| | | 6 | 4.70 | 110 | 5 | 1.9021 | 9 | 1.9015 | 023 |
| 22 | 4.40 | 34 | 4.39 | 101 | 5 | 1.8696 | 11 | 1.8685 | –313 |
| 3 | 4.33 | 3 | 4.32 | –111 | 2 | 1.8416 | 4 | 1.8407 | –322 |
| 8 | 3.614 | 5 | 3.617 | 111 | 1 | 1.8260 | 1 | 1.8252 | 032 |
| | | 6 | 3.600 | –102 | | | 1 | 1.8239 | –231 |
| 100 | 3.547 | 100 | 3.542 | –201 | 5 | 1.8108 | 7 | 1.8106 | –401 |
| 21 | 3.485 | 31 | 3.477 | 200 | 2 | 1.7769 | 5 | 1.7757 | 004 |
| 50 | 3.195 | 47 | 3.192 | 020 | 7 | 1.7368 | 11 | 1.7370 | 123 |
| 5 | 3.138 | 8 | 3.136 | –112 | 3 | 1.7040 | 5 | 1.7059 | 132 |
| 2 | 3.102 | 1 | 3.103 | 012 | | | 3 | 1.6996 | 231 |
| 1 | 3.059 | 1 | 3.054 | 210 | 12 | 1.6667 | 26 | 1.6665 | –323 |
| 16 | 2.935 | 30 | 2.931 | –202 | 2 | 1.6384 | 5 | 1.6386 | –403 |
| 23 | 2.910 | 20 | 2.911 | 021 | 11 | 1.5959 | 19 | 1.5958 | 040 |
| | | 12 | 2.901 | 120 | 2 | 1.5849 | 3 | 1.5826 | 033 |
| 38 | 2.855 | 44 | 2.854 | 102 | 4 | 1.5750 | 8 | 1.5748 | –421 |
| 30 | 2.804 | 39 | 2.803 | –121 | 1 | 1.5670 | 2 | 1.5656 | 114 |
| 2 | 2.668 | >1 | 2.664 | –212 | 2 | 1.5507 | 3 | 1.5517 | 024 |
| 12 | 2.607 | 19 | 2.606 | 112 | | | 2 | 1.5484 | –422 |
| 8 | 2.464 | 14 | 2.463 | –103 | 5 | 1.5209 | 12 | 1.5216 | 322 |
| 2 | 2.412 | 3 | 2.413 | –301 | 1 | 1.4984 | 2 | 1.4998 | 141 |
| 33 | 2.389 | 48 | 2.388 | –122 | 1 | 1.4621 | 2 | 1.4632 | 303 |
| 15 | 2.352 | 22 | 2.351 | 220 | 4 | 1.4549 | 6 | 1.4549 | –241 |
| 2 | 2.304 | 2 | 2.298 | –113 | 2 | 1.4395 | 5 | 1.4392 | –333 |
| 3 | 2.262 | 1 | 2.257 | –311 | 2 | 1.4301 | 5 | 1.4303 | –215 |
| 11 | 2.195 | 21 | 2.195 | 202 | 1 | 1.4010 | 3 | 1.4015 | –242 |
| 1 | 2.175 | 1 | 2.179 | 310 | 4 | 1.3923 | 8 | 1.3929 | 142 |
| 3 | 2.160 | 4 | 2.159 | –222 | | | 3 | 1.3927 | 214 |
| 10 | 2.126 | 7 | 2.128 | 122 | 1 | 1.3406 | 4 | 1.3428 | 332 |
| | | 8 | 2.125 | –312 | | | 5 | 1.3392 | –143 |
| 1 | 2.074 | 2 | 2.076 | 212 | 1 | 1.3148 | 2 | 1.3155 | –521 |
| 9 | 2.039 | 4 | 2.041 | 301 | 1 | 1.2907 | 3 | 1.2907 | 242 |
| | | 8 | 2.038 | 031 | | | | | |

658

659

660

661

662

663 **Table 7**. Raman frequencies ($cm^{-1}$) and band assignments for crocobelonite

664

| Crocobelonite-2*O* | Crocobelonite-1*M* | Assignment |
|---|---|---|
| 106, 147, 179, 239 | 131, 174, 191, 204, 237, 269, 339 | *M*–O bonds and lattice modes |
| 437, 471 | 379, 407, 431, 470 | Symmetric bending O–P–O |
| 508, 551, 570, 600, 640, 687, 805, 856 | 519, 532, 598, 630, 647 | Asymmetric bending O–P–O |
| 956, 989 | 951, 978 | Symmetric stretching O–P–O |
| 1022, 1083, 1143 | 1019, 1034, 1089, 1143 | Asymmetric stretching O–P–O |

665
666
667

This is the peer-reviewed, final accepted version for American Mineralogist, published by the Mineralogical Society of America.
The published version is subject to change. Cite as Authors (Year) Title. American Mineralogist, in press.
DOI: https://doi.org/10.2138/am-2022-8757. http://www.minsocam.org/

668

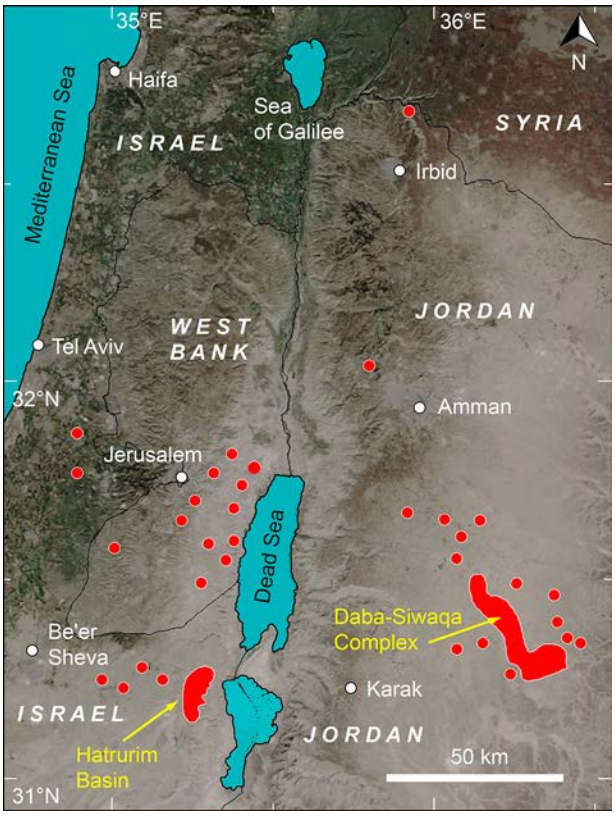


669

670 **Figure 1**

671

672

This is the peer-reviewed, final accepted version for American Mineralogist, published by the Mineralogical Society of America.
The published version is subject to change. Cite as Authors (Year) Title. American Mineralogist, in press.
DOI: https://doi.org/10.2138/am-2022-8757. http://www.minsocam.org/

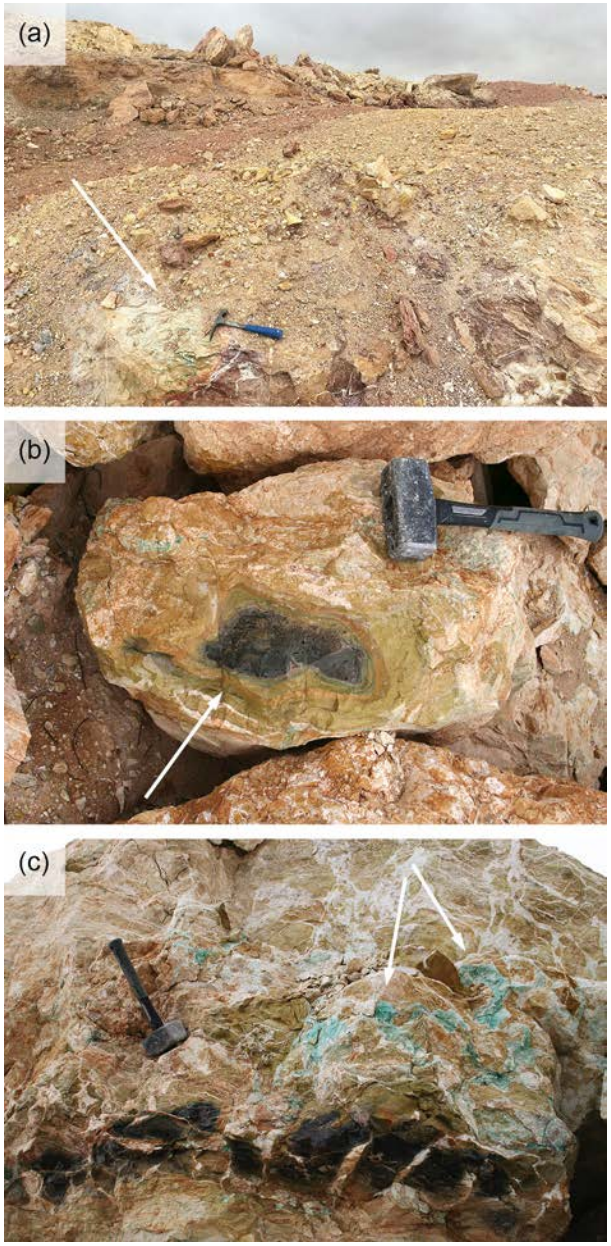


673

674 **Figure 2**

675

This is the peer-reviewed, final accepted version for American Mineralogist, published by the Mineralogical Society of America.
The published version is subject to change. Cite as Authors (Year) Title. American Mineralogist, in press.
DOI: https://doi.org/10.2138/am-2022-8757. http://www.minsocam.org/

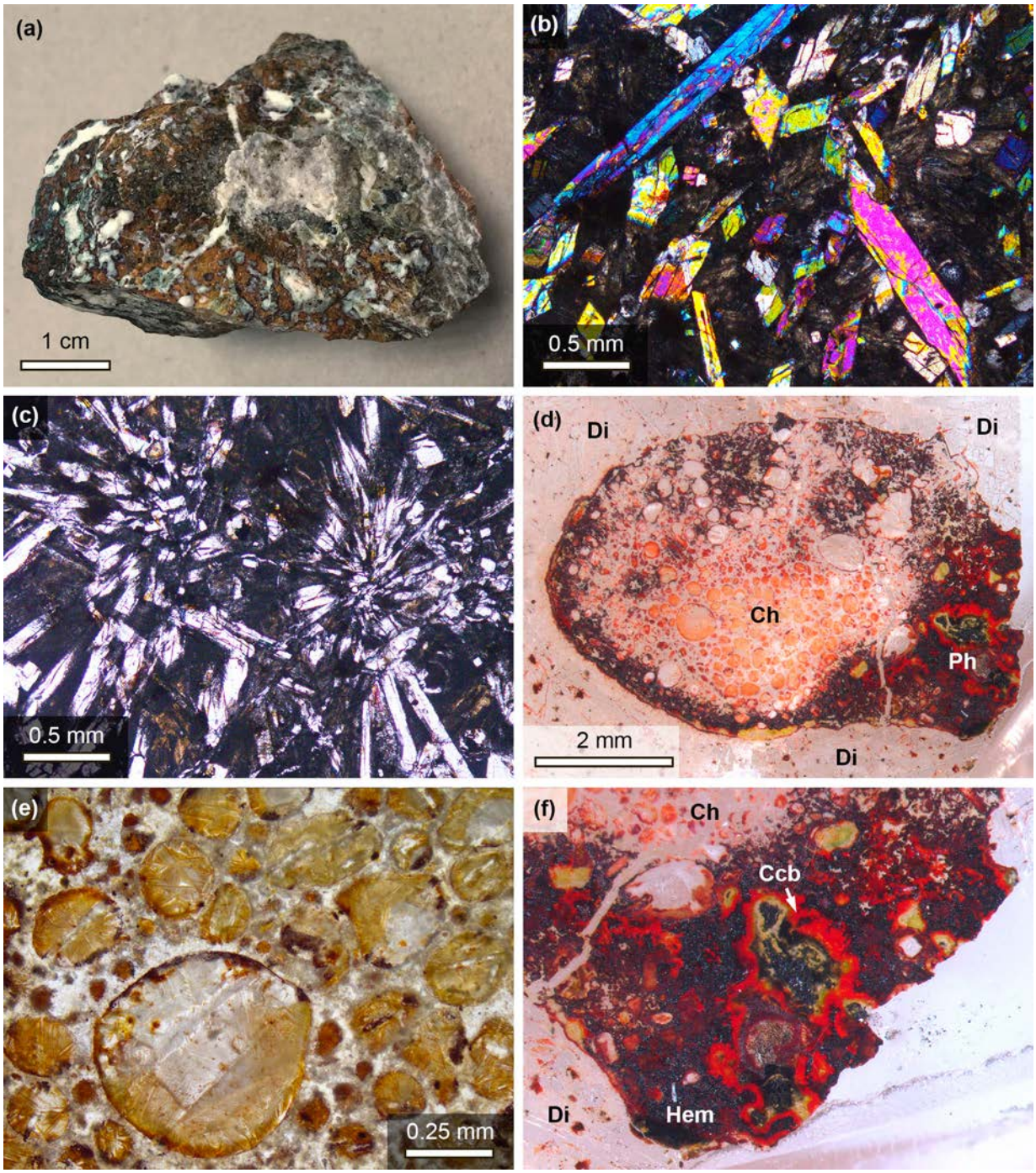


**Figure 3**

This is the peer-reviewed, final accepted version for American Mineralogist, published by the Mineralogical Society of America.
The published version is subject to change. Cite as Authors (Year) Title. American Mineralogist, in press.
DOI: https://doi.org/10.2138/am-2022-8757. http://www.minsocam.org/

680

681

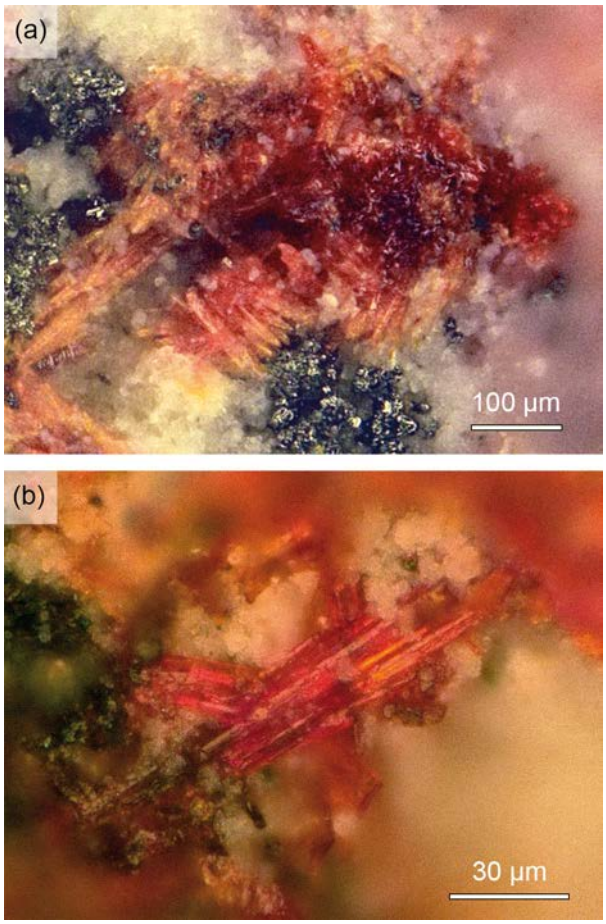


682

683 **Figure 4**

684

This is the peer-reviewed, final accepted version for American Mineralogist, published by the Mineralogical Society of America.
The published version is subject to change. Cite as Authors (Year) Title. American Mineralogist, in press.
DOI: https://doi.org/10.2138/am-2022-8757. http://www.minsocam.org/

685

686

687

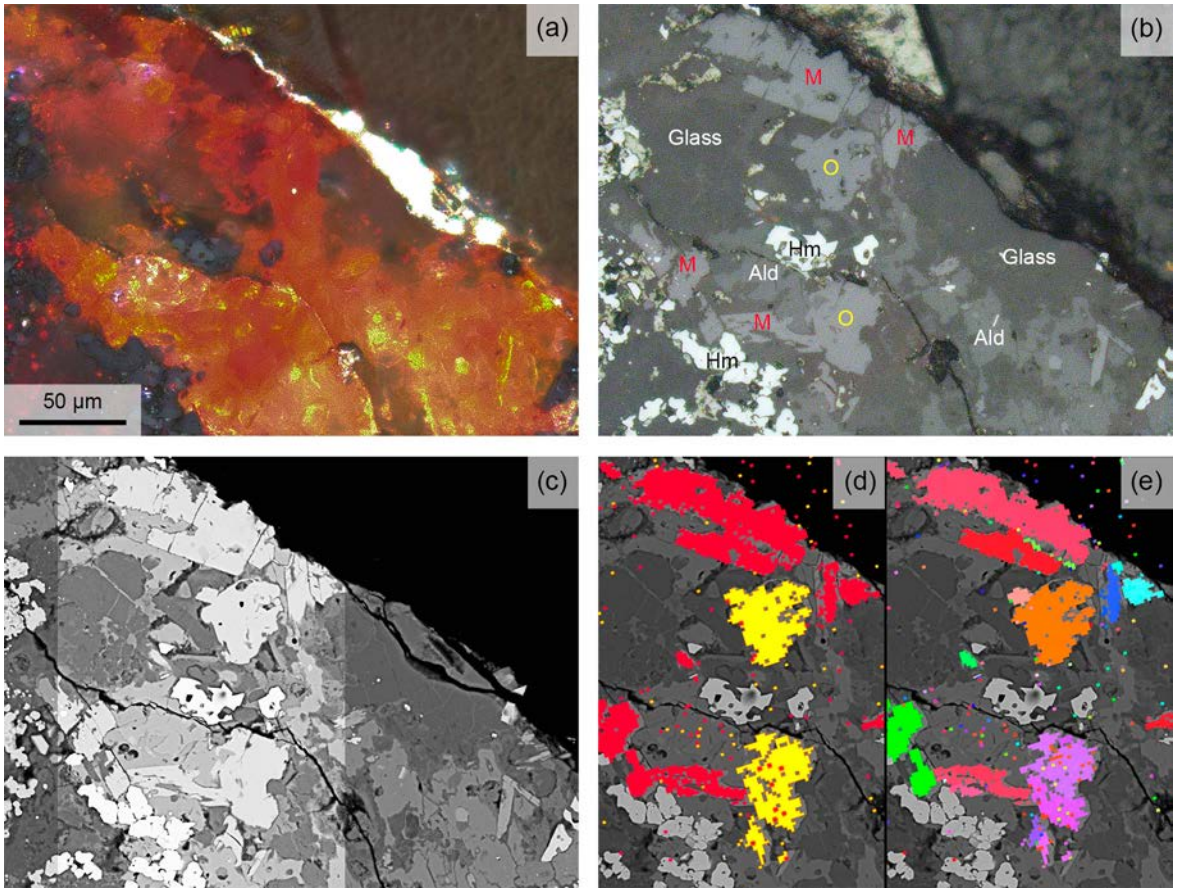


688

689 **Figure 5**

690

This is the peer-reviewed, final accepted version for American Mineralogist, published by the Mineralogical Society of America.
The published version is subject to change. Cite as Authors (Year) Title. American Mineralogist, in press.
DOI: https://doi.org/10.2138/am-2022-8757. http://www.minsocam.org/

691

692

693

694

695

696

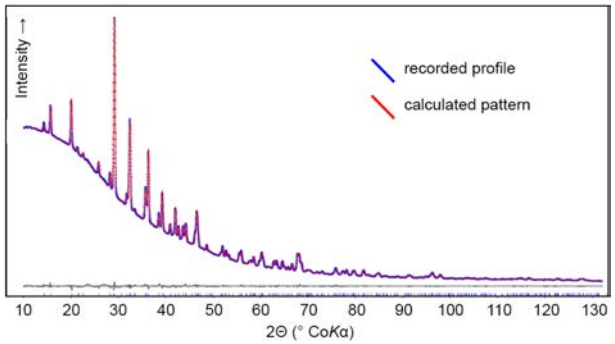


697

698 **Figure 6**

This is the peer-reviewed, final accepted version for American Mineralogist, published by the Mineralogical Society of America.
The published version is subject to change. Cite as Authors (Year) Title. American Mineralogist, in press.
DOI: https://doi.org/10.2138/am-2022-8757. http://www.minsocam.org/

699

700

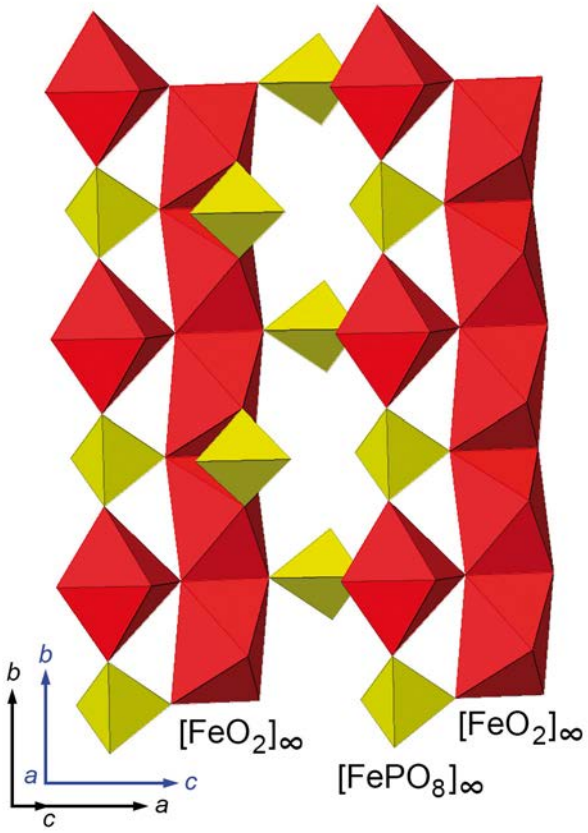


701

702 **Figure 7**

703

This is the peer-reviewed, final accepted version for American Mineralogist, published by the Mineralogical Society of America.
The published version is subject to change. Cite as Authors (Year) Title. American Mineralogist, in press.
DOI: https://doi.org/10.2138/am-2022-8757. http://www.minsocam.org/

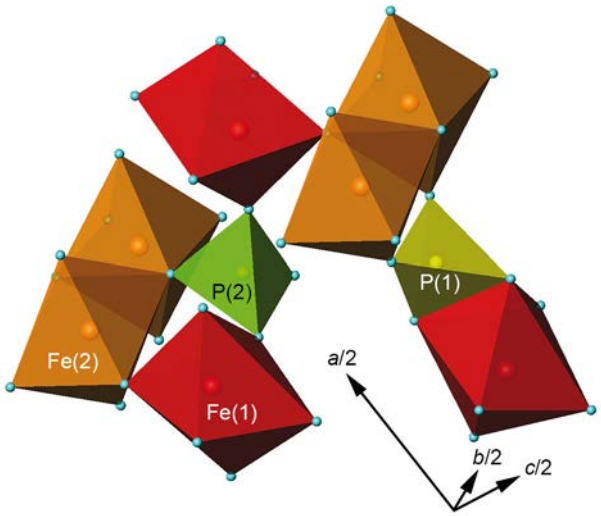


**Figure 8**

710

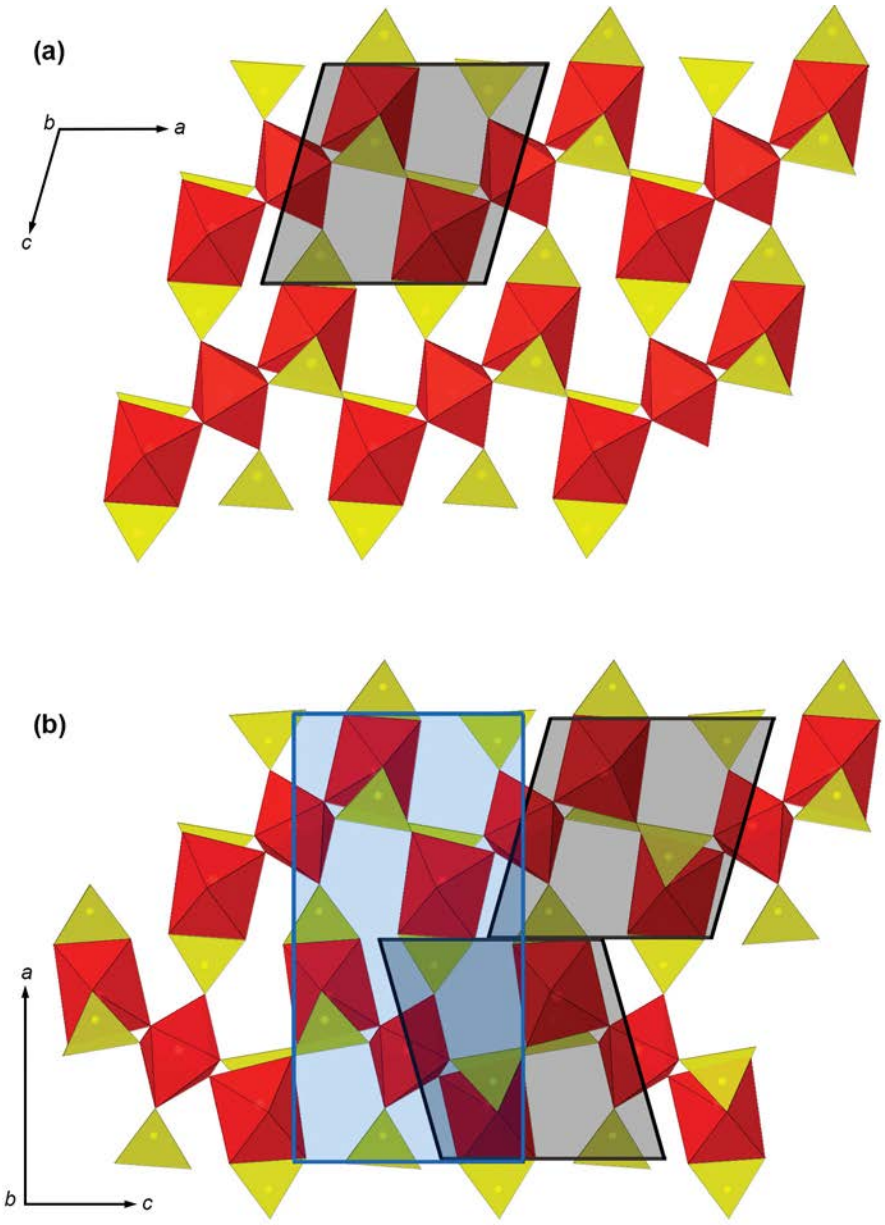


711

712 **Figure 9**

713

714

715

This is the peer-reviewed, final accepted version for American Mineralogist, published by the Mineralogical Society of America.
The published version is subject to change. Cite as Authors (Year) Title. American Mineralogist, in press.
DOI: https://doi.org/10.2138/am-2022-8757. http://www.minsocam.org/

716

717

718

719

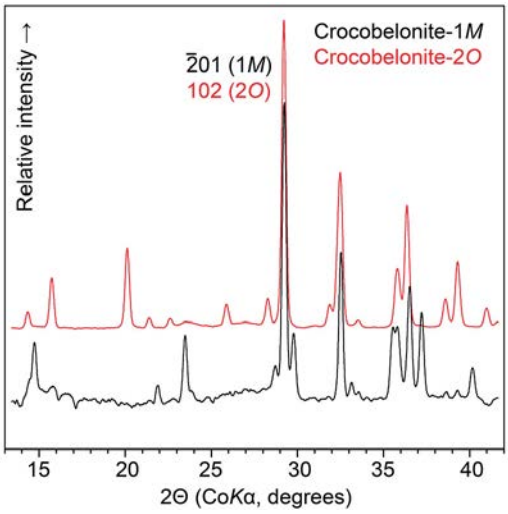


720

721 **Figure 10**.

722

This is the peer-reviewed, final accepted version for American Mineralogist, published by the Mineralogical Society of America.
The published version is subject to change. Cite as Authors (Year) Title. American Mineralogist, in press.
DOI: https://doi.org/10.2138/am-2022-8757. http://www.minsocam.org/

723

724

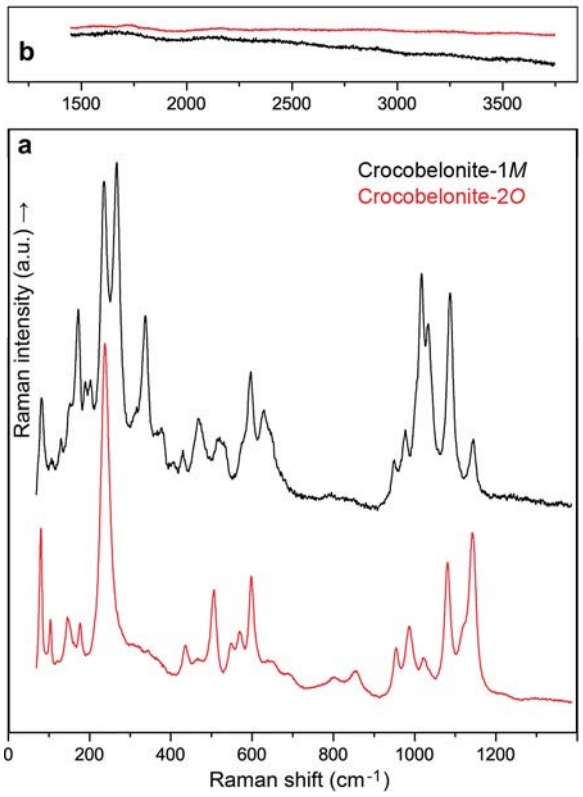


725

726 **Figure 11**

727